catalysts

MDPI

Article

Chemically Bonded N-PDI-P/WO_3 Organic-Inorganic Heterojunction with Improved Photoelectrochemical Performance

Cheng Feng †, Xihong Mi †, Dingwen Zhong, Weiming Zhang, Yongping Liu *, Dayong Fan, Ming Li, Jiefeng Hai and Zhenhuan Lu *

Guangxi Key Laboratory of Electrochemical and Magneto-Chemical Functional Materials, College of Chemistry and Bioengineering, Guilin University of Technology, Guilin 541004, China; fengcheng120612@163.com (C.F.); mxh1626568637@163.com (X.M.); ALSDWZ@163.com (D.Z.); zwm1002252523@163.com (W.Z.); dyfan@glut.edu.cn (D.F.); liming9989@163.com (M.L.); haijiefeng@glut.edu.cn (J.H.)

* Correspondence: liuyp624@163.com (Y.L.); zhenhuanlu@glut.edu.cn (Z.L.); Tel.: +86-773-253-8354 (Y.L. & Z.L.)

† These authors contributed equally to this work.

Received: 17 December 2019; Accepted: 13 January 2020; Published: 15 January 2020

Abstract: The chemical bonding of bandgap adjustable organic semiconductors with inorganic semiconducting materials is effective in constructing a high-performance heterogeneous photoanode. In this study, a new asymmetric perylene diimide derivative molecule (N-PDI-P) was synthesized by connecting tert-butoxycarbonyl on an N-site at one end of a PDI molecule through methylene and connecting naphthalene directly onto the other end. This molecule was bonded onto the WO_3 film surface, thereby forming the photoanode of organic-inorganic heterojunction. Under light illumination, the photocurrent density of chemically bonded N-PDI-P/WO_3 heterojunction was twofold higher than that of physically adhered heterojunction for photoelectrochemical water oxidation at 0.6 V (vs. Ag/AgCl). Energy band structure and charge transfer dynamic analyses revealed that photogenerated electron carriers on the highest occupied molecular orbital (HOMO) of an N-PDI-P molecule can be transferred to the conduction band of WO_3. The charge transfer and separation rates were accelerated considerably after the chemical bond formed at the N-PDI-P/WO_3 interface. The proposed method provides a new way for the design and construction of organic-inorganic composite heterojunction.

Keywords: perylene diimide; heterojunction; WO_3; photoelectrocatalysis; organic-inorganic composite

1. Introduction

The photoelectrocatalytic decomposition of water is an effective way to transform solar energy into an important clean energy, hydrogen [1–4]. However, the half-reaction of water decomposition at anodic oxidation is relatively slow, which is the main barrier of the entire reaction [5]. The development of high-activity photoanode has attracted wide attention. Several promising materials, such as black Si [6], $BiVO_4$ [7], TiO_2 [8,9], WO_3 [10], Fe_2O_3 [11,12], and ZnO [13], are topics that receive considerable attention in research. With an energy bandwidth of approximately 2.6 eV, WO_3, which is an important photoanode material, can absorb approximately 12% ultraviolet-visible light (UV-vis) in sunlight. WO_3 has a low valence band and a strong oxidizing capability in thermodynamics [14]. However, the electron–hole pairs, which are excited after illumination on WO_3, are easily combined, thereby leading to low photoelectric converting efficiency. Constructing heterojunction is an effective way of expanding the visible light (vis) absorption range and promoting light-induced charge separation of semiconductors [15–19].

With rich resources, easy structural modification, and large space for performance optimization, organics can compound with inorganic substances to offset the limitations of single inorganic semiconductors and improve the photocatalytic performance of the material [20,21]. As a classical N-type organic semiconductor material, perylene diimide derivative (PDI) has strong electronic delocalization capability, high-fluorescence quantum yield, and high molar absorption coefficient [22,23]. PDI has been widely applied in the semiconducting photoelectric field. The heterojunction of PDI that is bonded with $Zn_{0.5}Cd_{0.5}S$ can substantially improve photocatalytic H evolution performance [24]. The composite of PDI and Bi_2WO_6 can also improve photocatalytic O evolution [25]. The surface coverage of PDI can expand the visible light absorption range of inorganic semiconductors. Meanwhile, PDI with a large π system can expand the delocalization range of electrons to reduce electron–hole pairs. However, most of the existing organic-inorganic heterojunctions are physical bonding, thereby resulting in the low transmission efficiency of carriers and poor stability. These limitations can be offset by the chemical bonding of organic-inorganic heterojunction because of its perfect contact [26]. Nevertheless, it is relatively difficult to prepare organic-inorganic composites by chemical bonding.

In this paper, a new asymmetric PDI molecule (N-PDI-P, Scheme 1a) was synthesized based on molecular theory. Tert-butoxycarbonyl was connected onto one N-site of N-PDI-P via CH_2 to provide PDI molecule with the capability of bonding to metal oxides. Another N-site was connected with the naphthalene nucleus directly, which expanded the π conjugated system and strengthened light absorption. Next, N-PDI-P was bonded onto WO_3 film surface via a simple solution immersion method [27], thereby obtaining photoanode of the organic-inorganic molecular bonding heterojunction. The intermolecular bonding between organic and inorganic component was characterized. The photoelectrochemical performance of the constructed composite was investigated. The charge transfer of N-PDI-P/WO_3 interface was also studied. This new organic-inorganic composite heterojunction has promising application prospects in the field of high-efficiency photocatalytic material.

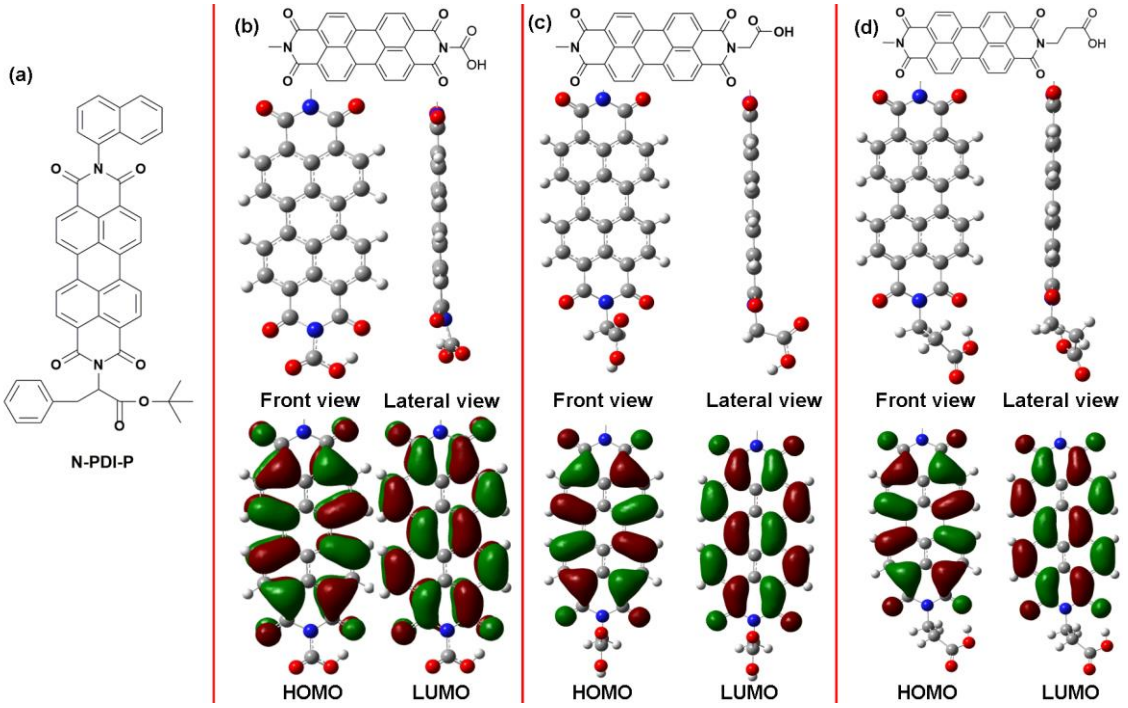

Scheme 1. (**a**) The molecular structure of N-PDI-P; Molecular calculation results of PDI molecules with (**b**) 0, (**c**) 1, and (**d**) 2 CH_2.

2. Results and Discussion

2.1. Design of N-PDI-P Molecule

The molecular structure of the target PDI derivatives was determined through theoretical computing. To study the effect of distance between N-sites of PDI and carboxyl on molecular performance, we carried out the theoretical computing simulation of PDI molecules with 0, 1, and 2 CH_2 between N-site and carboxyl by using density functional theory. Scheme 1 displays that substitution of N-site will not influence the planarity of molecules. Meanwhile, the HOMO and the lowest unoccupied molecular orbital (LUMO) of the PDI molecules remained almost unchanged. However, when directly connecting N-site to carboxyl, C atoms form C⁼⁼⁼N and C⁼⁼⁼O bonded conjugation, which may weaken the reaction activity of carboxyl further. Hence, the bonding between carboxyl and inorganic semiconducting materials, such as WO_3, is inhibited. The difference was that no conjugation occurred with at least one CH_2 that was present between N-site and carboxyl. Theoretically, a prolonged C chain may increase the distance for electron transmission between PDI and inorganic semiconducting materials. As a result, PDI with one CH_2 between N and carboxyl was synthesized in the present study.

A new asymmetric molecule (N-PDI-P) was synthesized according to the path in Figure S1. One N-site of N-PDI-P molecule was coupled with naphthyl, and another was connected with tert-butoxycarbonyl and benzyl simultaneously through a methylene. Specifically, naphthyl expanded the π system, whereas tert-butoxycarbonyl and benzyl improved the solubility of molecules.

2.2. Characterization of Intermolecular Bonding between Organic and Inorganic Molecules

Scanning electron microscope (SEM) images are shown in Figure 1a. WO_3, which is obtained through anodization, is a nanofilm with pore structures. A thin layer of uniform N-PDI-P organic film can be covered onto WO_3 nanofilm by infiltrating in the $CHCl_3$ solution of N-PDI-P for one day (Figure 1b). SEM images determined that N-PDI-P film is uniform in a large area and thickened as the infiltration time increased (Figure 1c–j). Film thickness measurement results showed that the film thickness of N-PDI-P increased with the infiltration days from 1 to 6. According to the energy disperse spectroscopy (Figure 1k–n and Supplementary Materials Figure S2), a WO_3 nanofilm surface was covered with a layer of C-containing organics uniformly.

The composite was scraped from tungsten base and ultrasonic dispersion in absolute ethyl alcohol and then observed under transmission electron microscopy (TEM, Figure 2a,b). Many black particles were scattered on the organic film. In the amplification images, lattice spacing corresponded to the diffraction peak of the XRD crystal face of WO_3. Thus, 0.368 nm corresponds to the (020) crystal spacing of WO_3, and 0.379 nm corresponds to (002). In particular, a tight cohesion between WO_3 and N-PDI-P organic film was observed clearly at the position of arrow (Figure 2a), which can be maintained after ultrasonic vibration. This result proved that organics and inorganics can form extremely strong chemical adsorption.

The diffraction peak of WO_3 corresponded to the crystal face diffraction peak in monoclinic crystal WO_3 (Figure 2c) [10]. Two strong diffraction peaks at 58.20° and 73.17° were the characteristic peaks of the base W. The diffraction peak intensity of WO_3 decreased slightly after bonding with N-PDI-P, which was the consequence of N-PDI-P coverage. No evident aromatic ring's π–π accumulation peak was observed, thereby indicating that N-PDI-P in the composite failed to form a good crystal type.

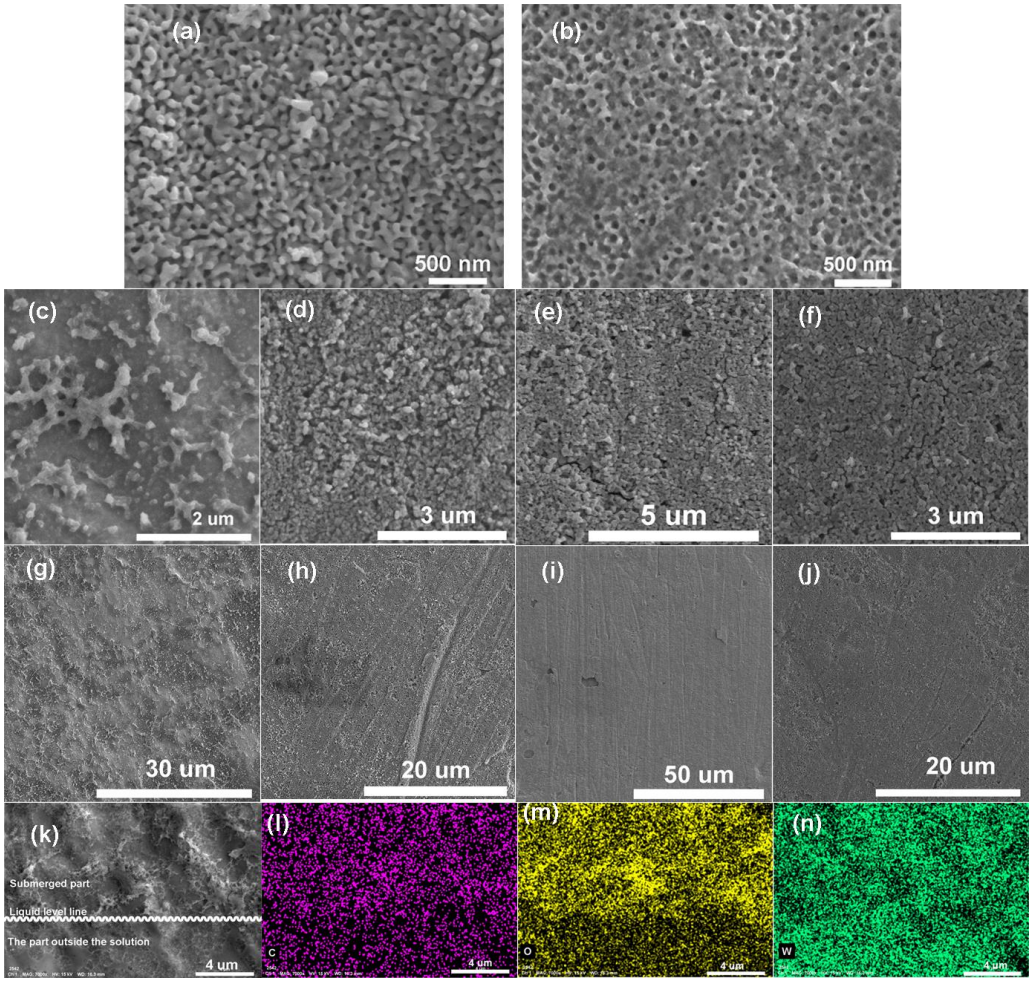

Figure 1. SEM images of (**a**) WO_3, N-PDI-P/WO_3 after (**b**) 1 d, (**c**,**g**) 2 d, (**d**,**h**) 3 d, (**e**,**i**) 4 d, (**f**,**j**) 5 d infiltration; (**k**) SEM image of N-PDI-P/WO_3 composite sample prepared by infiltration for 1 d and EDS spectroscopy with elemental mapping of (**l**) C, (**m**) O, (**n**) W.

To prevent the poor expression of bonding information on interface due to the thick N-PDI-P layer, we chose the sample with the thinnest N-PDI-P layer after one day of infiltration for structural characterization. Figure S3a presents a high-resolution survey spectrum of the composite, indicating the presence of W, C, and O. Figure S3b shows the high-resolution X-ray photoelectron spectroscopy (XPS) spectrum corresponding to the W of N-PDI-P/WO_3 composite. Two main XPS peaks are ascribed to the typical doublet of W^{6+} with the binding energy of W ($4f_{7/2}$) at 35.1 eV, and W ($4f_{5/2}$) at 37.3 eV. The peak ratio of W ($4f_{7/2}$) to W ($4f_{5/2}$) is 4:3. A third broad peak of W ($5p_{3/2}$) locates at ~41 eV. The high-resolution XPS spectrum of N-PDI-P/WO_3 reveals only a W^{6+} oxidation state. The O-1s core-level spectra of WO_3 nanofilm and N-PDI-P/WO_3 are shown in Figure 2d,e. The O (1s) XPS spectra of WO_3 exhibit asymmetric line shapes and the peaks are fitted with two components. One main peak at 530.5 eV corresponds to the W-O bond, and the other at 531.8 eV corresponds to -OH groups due to atmospheric contamination or the crystal water. Figure 2e shows that the above-mentioned peaks of WO_3 in N-PDI-P/WO_3 composite were extremely low. According to our previous work [28], the C = O peak of the ester group was 532.21 eV, and the C–O–C peak was observed at 532.64 eV, but only an extremely low wide peak near 532.5 eV can be found in this composite. Meanwhile, a significant metal carboxylate peak was observed at 531.4 eV, which belonged to the C–O–W peak. This result proved that N-PDI-P and WO_3 can be bonded through carboxyl [29].

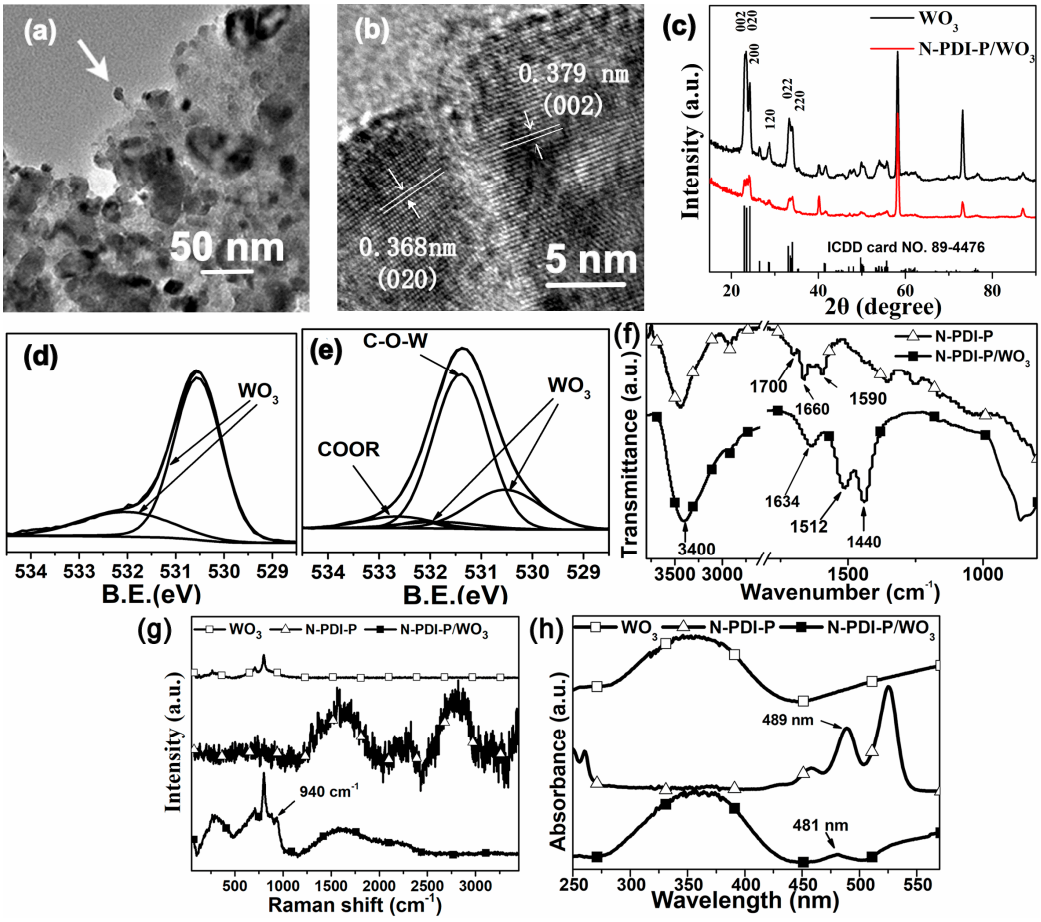

Figure 2. (**a**,**b**) TEM images and (**c**) XRD spectra of N-PDI-P/WO_3 after 1 d infiltration; the O 1s XPS spectra of (**d**) WO_3 and (**e**) N-PDI-P/WO_3 after 1 d infiltration; (**f**) Infrared spectroscopy, (**g**) Raman spectrum, and (**h**) UV-vis DRS curve of WO_3, N-PDI-P, and N-PDI-P/WO_3.

The infrared spectra of N-PDI-P and N-PDI-P/WO_3 composite were compared (Figure 2f). The C=O characteristic adsorption peak of tert-butoxycarbonyl in N-PDI-P was observed at 1700 cm^{-1}, while the C=O peak in the composite disappeared considerably. New adsorption peaks were observed at 1634 and 1440 cm^{-1}, which were the antisymmetrical and symmetrical stretching vibration peaks of O⁼⁼⁼C⁼⁼⁼O in carboxylate, respectively [30]. This observation reflected that N-PDI-P bonded onto the WO_3 surface successfully. According to Raman spectra (Figure 2g), N-PDI-P had a characteristic C–H adsorption peak at 2800 cm^{-1}, a characteristic C–N adsorption peak at 2260 cm^{-1}, a characteristic C=O adsorption peak on aromatic at 1620 cm^{-1}, and a characteristic C–O–C adsorption peak on tert-butoxycarbonyl at 690 cm^{-1}. WO_3 nanofilm had evident adsorption peaks at 269, 713, and 806 cm^{-1}, which belonged to its lattice vibration. However, the composite had a new peak at 940 cm^{-1}, which showed the formation of a new bond, which may be caused by the vibration coupling of O⁼⁼⁼C⁼⁼⁼O of carboxylate. Hence, N-PDI-P is bonded onto the WO_3 surface through carboxyl successfully. UV-vis diffuse reflectance (Figure 2h) showed that the λ_{edge} of WO_3 edge was approximately 446 nm, and the composite produced a small red shift (approximately 455 nm). The adsorption peaks of N-PDI-P were in the range of 450–550 nm, which proved the improved absorbance of the composite. One shoulder peak with uncertain peak position was observed in the range of 510–530 nm, which corresponded to the peak of N-PDI-P at 525 nm. N-PDI-P had a characteristic peak at 489 nm, which produced a blue shift to 481 nm after bonding, thereby showing that solid organic molecules were formed by an H-aggregate [31].

2.3. Performance of N-PDI-P/WO_3 Organic-Inorganic Heterojunction

To explore the influence of intermolecular forces on photoelectric catalytic performance, we prepared the sample of physically adsorbed N-PDI-P on WO_3 called WO_3-Spin by dropping the N-PDI-P solution (in chloroform) on the unprocessed WO_3 film and then drying naturally after wetting uniformly. The linear sweep voltammetry (LSV) and current–time (I–t) curves in Figure 3a,b, respectively, showed that the photocurrent of WO_3-Spin was similar to WO_3 film, that is, approximately 0.31 milliampere per square centimeter (mA/cm^2) under 0.6 V bias voltage (vs. Ag/AgCl). The photocurrent of N-PDI-P/WO_3 was much higher than those of WO_3 and WO_3-Spin composite film. This result demonstrated that chemical bonding tightened the combination of N-PDI-P and WO_3, which were conducive for charge transfer at the interface. Given the bias voltage of 0.6 V (vs. Ag/AgCl), the photocurrent densities of N-PDI-P/WO_3 heterojunction after 1, 2, 3, 4, 5, and 6 days of infiltration are 0.44, 0.47, 0.52, 0.61, 0.54, and 0.52 mA/cm^2, respectively. The photocurrent of heterojunction increased was positively related to N-PDI-P film thickness. The photocurrent density of N-PDI-P/WO_3 composite reached the peak after four days of infiltration. This phenomenon may be because the light adsorption of WO_3 was inhibited when the N-PDI-P film was extremely thick, which decreased the photocurrent. Figure 3b shows that the photocurrent does not attenuate after 10 min of light irradiation at 0.6V bias voltage (vs. Ag/AgCl), which indicates that the constructed N-PDI-P/WO_3 heterojunction has good stability. According to the alternating current impedance test (Figure 3c,d), the impedance of N-PDI-P/WO_3 composite under illumination and dark conditions was smaller than that of WO_3 film. The results show that impedance gradually decreases from 1 to 4 infiltration days and increases from 5 to 6 days. Such advantage was apparent under illumination conditions probably because the excited electron separation efficiency increased, the recombination rate of electron-hole pairs decreased, and the photocurrent was strengthened due to the bonding between N-PDI-P and WO_3.

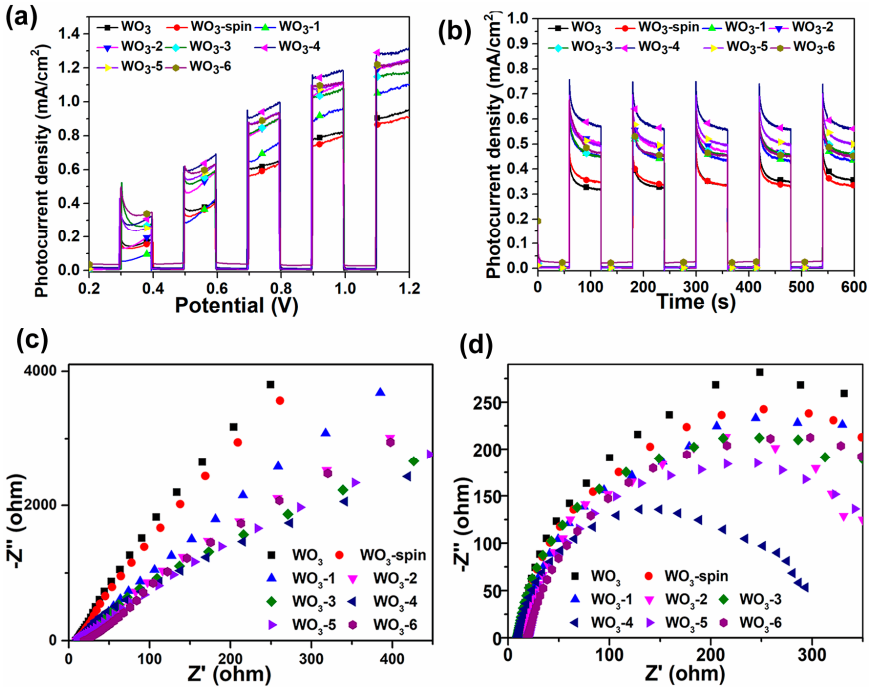

Figure 3. (**a**) linear sweep voltammetry (LSV) and (**b**) current–time (I–t) curve of N-PDI-P/WO_3 composite materials; electrochemical impedance spectroscopy (EIS) of WO_3 films and N-PDI-P/WO_3 composite materials under (**c**) dark and (**d**) light conditions. WO_3 represents a pure WO_3 sample; WO_3-1, WO_3-2, WO_3-3, WO_3-4, WO_3-5, and WO_3-6 represent N-PDI-P/WO_3 composite materials, which were prepared by 1, 2, 3, 4, 5, and 6 days of infiltration.

2.4. Charge Transfer of N-PDI-P/WO_3 Organic-Inorganic Interface

The incident-photon-to-current-conversion efficiency (IPCE) measurement was measured at 0.6V vs. Ag/AgCl according to the equation: IPCE = (1240 × J)/(λ × I_0), where J is the photocurrent density (mA/cm^2), λ is the incident wavelength, and the I_0 is the incident light intensity (mW/cm^2) [9]. As shown in Figure 4a, the IPCE curves of the WO_3 and N-PDI-P/WO_3 composite have a similar shape. For N-PDI-P/WO_3 composite, IPCE keeps on increasing from 350 nm to 600 nm. The IPCE for N-PDI-P/WO_3 composite shows a maximum efficiency of about 19.1% at a wavelength of 370 nm, which is about 1.91 times higher than that of WO_3 (10.0%). This clearly shows that, when WO_3 is chemically bonded with N-PDI-P, there is a significant enhancement in the IPCE due to efficient separation of photogenerated excitons at the N-PDI-P/WO_3 interface.

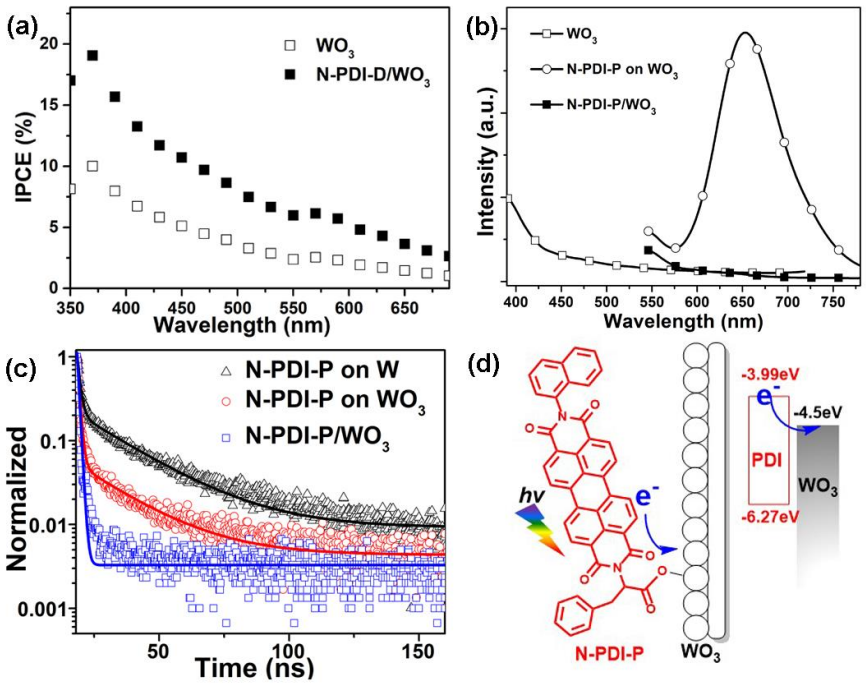

Figure 4. (**a**) IPCE of WO_3 and N-PDI-P/WO_3 composite; (**b**) steady-state photoluminescence of WO_3, WO_3 with physical adsorption of N-PDI-P film and N-PDI-P/WO_3 Heterojunction; (**c**) TRPL of W, WO_3 with physical adsorption of N-PDI-P film and N-PDI-P/WO_3 composite; (**d**) schematic of charge transfer at the N-PDI-P/WO_3 interface.

The HOMO and LUMO of N-PDI-P were calculated to study the direction of electron transfer. The UV-vis adsorption normalized curve of the CH_2Cl_2 solution (1×10^{-4} mol/L) of N-PDI-P is shown in Figure S4a. This molecule had three classical characteristic adsorption peaks of PDI in the range of 440–560 nm, and the optical band gap was E_{optg} = 2.28 eV [32]. The cyclic voltammetry curve of N-PDI-P is shown in Figure S4b. Hence, HOMO = −6.27 eV and LUMO = −3.99 eV. However, the conduction band (CB) edge position of WO_3 was in the region of 0V relative to NHE, which was converted to a vacuum level of −4.5 eV. This result matched well with the LUMO of N-PDI-P. Electron carriers produced by N-PDI-P after illumination can be transferred to WO_3, thereby increasing the photocurrent density of composite.

To demonstrate the electron-transfer dynamics from N-PDI-P to the W and WO_3 interface further, we carried out steady-state and time-resolved photoluminescence (PL) measurements. The details of the steady-state PL spectra are provided in Figure 4b. WO_3 had no apparent fluorescence after $\lambda_{max\text{-}absorb}$ excitation (370 nm). By contrast, the sample prepared through physical adsorption (abbreviated as WO_3-Spin) produced fluorescence at 658 nm after excitation at 525 nm. The N-PDI-P/WO_3 composite that was prepared by the proposed infiltration method developed fluorescence quenching after

excitation at 525 nm. Time-resolved PL (TRPL) measurements (Figure 4c) showed the normalized decay profiles after pulsed laser excitation at 658 nm for a series of samples. The results demonstrate that TRPL of all three samples are dominated by short decay lifetime (see Supplementary Materials Table S1). The average lifetimes were found to be 1.18 microsecond (μs) for N-PDI-P on W, 1.11 μs for N-PDI-P on WO_3, and 0.75 μs for N-PDI-P/WO_3 composite. These findings proved that the electrons excited by N-PDI-P can be transferred onto WO_3. Electron transfer accelerated considerably after the chemical bonding of N-PDI-P and WO_3, thereby increasing photocurrent accordingly.

Based on the above results, a schematic illustration of the charge transfer process responding to the enhanced photocurrent density of N-PDI-P/WO_3 heterojunction photoanode is depicted in Figure 4d. Once N-PDI-P/WO_3 heterojunction is illuminated, the electrons in the LUMO of N-PDI-P are excited to its HOMO. Then, the photogenerated electrons within the HOMO of N-PDI- can be easily moved to the CB of WO_3, which could be driven by the formed chemical bond and the matched energy level between N-PDI-P and WO_3. The excited electrons in WO_3, which include the excited electrons of N-PDI-P and WO_3 itself, are collected onto the W base. As a result, the photocurrent density of the chemically bonded N-PDI-P/WO_3 composite increased significantly compared with WO_3.

3. Materials and Methods

3.1. General Procedure for Synthesis of N-PDI-P

Firstly, 3,4,9,10-Perylenetetracarboxylic dianhydride was hydrolyzed in KOH solution, and then esterified with 1-bromohexane. Secondly, the mono-side anhydride product was synthesized under the catalytic condition of *p*-toluene sulfonic acid; thirdly, the mono-side anhydride product was reacted with naphthylamine to obtain the mono-side imide product; finally, the mono-side imide product was anhydrided by *p*-toluene sulfonic acid and imidized with L-phenylalanine tert-butyl ester to obtain the final product N-PDI-P. ^{1}H NMR (500 MHz, $CDCl_3$) δ ppm: 8.74 (d, 2H), 8.62 (d, 2H), 8.57 (q, 4H), 7.43–8.00 (m, 7H), 7.07–7.23 (m, 5H), 6.00 (dd, 1H), 3.71 (dd, 1H), 3.53 (dd, 1H), 1.50 (s, 9H); ^{13}C NMR (126 MHz, $CDCl_3$) δ ppm: 168.41, 163.64, 162.89, 135.18, 134.78, 132.09, 131.70, 130.10, 129.71, 129.21, 128.31, 127.26, 126.79, 126.46, 125.66, 123.56, 123.20, 123.01, 121.80, 82.25, 55.40, 35.02, 28.01; MS (MALDI-TOF): m/z = 720.2 $[M]^+$; Elemental analysis: calcd (%) for $C_{47}H_{32}N_2O_6$: C 78.32, H 4.48, N 3.89; found C 78.53, H 4.46, N 4.10. Specific reagent concentration and procedures are detailed in the Supporting Information.

3.2. Preparation of N-PDI-P/WO_3 Organic-Inorganic Heterojunction

The WO_3 nano film was prepared by a pulse anodic oxidation method, which is described in our previous work [33].

We utilized a N-PDI-P bond with WO_3 by taking advantage of tert-butoxy in this ester group, which can be easily replaced by a nucleophile (e.g., alkoxy anion). After one hour of the ultraviolet ozone pre-treatment, the WO_3 Nano film was infiltrated into a hexane solution with $(CH_3)_3COLi$ (1.0 mol/L) for 48 h for deprotonation of OH groups on WO_3 nanofilm. The activated O anions can attack the ester groups of N-PDI-P and replace tert-Butoxy to produce carboxylate. After the above activation, the treated WO_3 nanofilm was washed with n-hexane and naturally dried, and then infiltrated into the chloroform solution of N-PDI-P (1.0×10^{-4} mol/L) for 1–6 days in the dark. Finally, the sample was washed with absolute ethanol and dried at 60 °C to obtain the final product. During these processes, N-PDI-P can be bonded onto the WO_3 nanofilm, and the photoanode material of the chemically bonded organic-inorganic heterojunction was obtained. All of the operations were carried out in a dry atmosphere glovebox.

3.3. Calculation, Characterization, and Measurements

Density functional theory (DFT) calculations were performed with the Gaussian 09 program, using the B3LYP functional. All-electron double-ξ, valence basis sets with polarization functions

6-31G* were used for all atoms; ^{1}H NMR and ^{13}C NMR spectrums were recorded by a Varian Inova 500 NMR spectrometer (Palo Alto, CA, USA) with $CDCl_3$ as a solvent and tetramethylsilane (TMS) as an internal reference; MALDI-TOF mass spectra were recorded by a Bruker BIFLEXIII (Bremen, Germany); Elemental analysis was performed on a flash EA1112 analyzer; the XRD patterns were recorded using a PANalytical X'Pert^3 powder diffractometer (Almelo, The Netherlands) with Cu Kα radiation (λ = 1.54056 Å); The scanning electron microscopy (SEM) images were taken on a JSM-638OLV scanning electron microscope (Tokyo, Japan) equipped with an energy-dispersive X-ray spectroscopy (EDS) detector (Tokyo, Japan); Film thickness measurement was performed with an AMBIOS Surface Profilomer XP-2 (Santa Cruz, CA, USA); the transmission electron microscopy (TEM) images were obtained with a JEOL Model JEM-2100F (Tokyo, Japan); X-ray photoelectron spectroscopy (XPS) spectra were measured on an ESCALAB 250XI electron spectrometer from Thermo Scientific (Madison, WI, USA) with an AlKα source (photoelectron energy: 1253.6 eV); and the Fourier Transform infrared spectroscopy (FT-IR) was tested in a 400–4000 cm^{-1} wavenumber using a Nicolet IS10 Fourier Infrared Spectrometer (Madison, WI, USA). When preparing the sample, the composite material was scraped off from the surface of the sample, and after KBr was mixed, the mixture was tableted for testing; Raman spectra were recorded on a Renishaw inVia raman microscope system using Ar^+ laser (532 nm, 20 mW) for excitation; the photoluminescence spectra with an excitation wavelength of 525 nm were recorded on a F1-4600 (Hitachi) fluorescence spectrophotometer (Tokyo, Japan); diffuse reflectance spectra (DRS) of the film samples were obtained with a UV/VIS/NIR spectrometer (Lambda 750, PerkinElmer, Waltham, MA, USA). $BaSO_4$ was used as the standard reflectance material. The ultraviolet-visible spectroscopy (UV-vis) of the N-PDI-P (1×10^{-4} mol/L, CH_2Cl_2 as a solvent) was obtained in the range 200–800 nm; the photoelectrochemical measurements were carried out using an electrochemistry station (CHI860D) with three-electrode system (film samples as the working electrodes, platinum counter electrode, and Ag/AgCl (saturated) reference electrode). The measurements were conducted using 0.5M Na_2SO_4 aqueous solution as an electrolyte under an illumination of solar simulator (Newport Oriel 91192, Stratford, CT, USA) at 100 mW/cm^2, and the active area was 1 cm^2. The incident photon to electron conversion efficiency (IPCE) was estimated from chronoamperometry measurements at a bias potential of 0.6 V vs. Ag/AgCl in 0.5 M Na_2SO_4, by using a 300 W Xe lamp (Beijing Perfect Light Technology Co., LS-SXE300, China) coupled with a monochromator (Beijing Au Light Co., CEL-IS151). The electrochemical cyclic voltammetry (CV) was performed using a CHI860 electrochemical workstation in a potassium ferricyanide aqueous solution (2 mmol/L $K_3Fe(CN)_6$, 1mol/L KNO_3) with a scan speed at 0.1 V/s. A Pt wire and Ag/AgCl were used as the counter and reference electrodes, respectively. The reference value (Ag/AgCl), which is used for the estimation of HOMO and LUMO energy values, is −4.4 eV vs. vacuum; time-resolved photoluminescence (TRPL) measurements were carried out using transient/steady-state fluorescence spectrophotometer (FLS920, Edinburgh Instruments, Scotland, UK). The data may be fitted by either single- or double-exponential decay kinetics (formula (1)); the average lifetimes can be calculated using formula (2). A_n is the amplitude of lifetime component τ_n, τ is the lifetime value:

$$y = y_0 + \sum A_n e^{-X/\tau_n} (n = 1, 2), \quad (1)$$

$$\tau = \sum A_n \tau_n^2 / A_n \tau_n (n = 1, 2). \quad (2)$$

4. Conclusions

In summary, a new N-PDI-P molecule was synthesized in this study. WO_3 nanofilm was prepared by the microarc oxidation technique. After activation, the WO_3 nanofilm surface produced O anion, which attacked the ester group of N-PDI-P and replaced tert-butoxy to produce carboxylate, thereby forming organic-inorganic heterojunction. Raman, XPS, and FT-IR characterizations proved that N-PDI-P molecules were bonded onto metallic oxide surface through ester groups. The photocurrent density of the chemically bonded N-PDI-P/WO_3 composite (0.61 mA/cm^2) increased more significantly compared with WO_3 (0.31 mA/cm^2) at 0.6 V (vs. Ag/AgCl). According to energy band structure analysis,

the HOMO and LUMO of N-PDI-P molecule matched well with those of WO_3, that is, the electron can transfer from the HOMO of N-PDI-P to the CB of WO_3. The dynamic analysis demonstrated that the charge transfer and separation were accelerated significantly by the chemical bond of the N-PDI-P/WO_3 interface, which was beneficial for the improved efficiency of photoelectrochemical water decomposition. The proposed method provided a new way for organic-inorganic heterojunction synthesis and offered important references for the development of high-efficiency photocatalytic materials.

Supplementary Materials: The following are available online at http://www.mdpi.com/2073-4344/10/1/122/s1, Figure S1: Synthetic Route for N-PDI-P, Figure S2: (a) SEM images of PDI-WO3 composites prepared by immersion for four days and EDS spectroscopy with elemental mapping of (b) C, (c) O, (d) W, and (e) N, Figure S3: XPS spectra: (a) survey spectrum of the prepared N-PDI-P/WO3 composite and high-resolution spectra showing (b) the W 4f7/2, W 4f5/2 and W 5p3/2 peaks, Figure S4: (a) UV-Vis curve and (b) CV curve of N-PDI-P, Figure S5: The 1H NMR spectra of N-PDI-P, Figure S6: The 13C NMR spectra of N-PDI-P, Figure S7: The MS spectra of N-PDI-P, Table S1: Decay times measured around the PL peak from time-resolved PL for N-PDI-P on W, N-PDI-P on WO_3 and N-PDI-P/WO_3.

Author Contributions: C.F. and X.M. designed, administered, and performed the experiments; D.Z. and W.Z. performed the organic synthesis; D.F., M.L., and J.H. collected and analyzed data. Y.L. and Z.L. discussed the data and wrote the manuscript. All authors have read and agreed to the published version of the manuscript.

Funding: This work was supported by the National Natural Science Foundation of China (No. 21563007, 21962005), the Guangxi Natural Science Foundation (No. 2018GXNSFAA281137, 2017GXNSFAA198343, 2015GXNSFBA139021), and Guangxi Key Laboratory of Electrochemical and Magnetochemical Functional Materials (No. EMFM20181105).

Conflicts of Interest: The authors declare no conflict of interest.

References

1. Ouyang, T.; Ye, Y.-Q.; Wu, C.-Y.; Xiao, K.; Liu, Z.-Q. Heterostructures Composed of N-Doped Carbon Nanotubes Encapsulating Cobalt and β-Mo_2C Nanoparticles as Bifunctional Electrodes for Water Splitting. *Angew. Chem. Int. Ed.* **2019**, *58*, 4923–4928. [CrossRef]
2. Ge, J.; Yin, W.-J.; Yan, Y. Solution-Processed Nb-Substituted $BaBiO_3$ Double Perovskite Thin Films for Photoelectrochemical Water Reduction. *Chem. Mater.* **2018**, *30*, 1017–1031. [CrossRef]
3. Xu, S.; Fu, D.; Song, K.; Wang, L.; Yang, Z.; Yang, W.; Hou, H. One-dimensional WO_3/$BiVO_4$ heterojunction photoanodes for efficient photoelectrochemical water splitting. *Chem. Eng. J.* **2018**, *349*, 368–375. [CrossRef]
4. Landman, A.; Dotan, H.; Shter, G.E.; Wullenkord, M.; Houaijia, A.; Maljusch, A.; Grader, G.S.; Rothschild, A. Photoelectrochemical water splitting in separate oxygen and hydrogen cells. *Nat. Mater.* **2017**, *16*, 646–651. [CrossRef]
5. Klepser, B.M.; Bartlett, B.M. Anchoring a Molecular Iron Catalyst to Solar-Responsive WO_3 Improves the Rate and Selectivity of Photoelectrochemical Water Oxidation. *J. Am. Chem. Soc.* **2014**, *136*, 1694–1697. [CrossRef] [PubMed]
6. Yu, Y.; Zhang, Z.; Yin, X.; Kvit, A.; Liao, Q.; Kang, Z.; Yan, X.; Zhang, Y.; Wang, X. Enhanced photoelectrochemical efficiency and stability using a conformal TiO_2 film on a black silicon photoanode. *Nat. Energy* **2017**, *2*, 17045. [CrossRef]
7. Kim, T.W.; Choi, K.S. Nanoporous $BiVO_4$ photoanodes with dual-layer oxygen evolution catalysts for solar water splitting. *Science* **2014**, *343*, 990–994. [CrossRef] [PubMed]
8. Chen, X.; Liu, L.; Huang, F. Black titanium dioxide (TiO_2) nanomaterials. *Chem. Soc. Rev.* **2015**, *44*, 1861–1885. [CrossRef] [PubMed]
9. Lin, J.; Liu, Y.; Liu, Y.; Huang, C.; Liu, W.; Mi, X.; Fan, D.; Fan, F.; Lv, H.; Chen, X. SnS_2 Nanosheets/H-TiO_2 Nanotube Arrays as a Type II Heterojunctioned Photoanode for Photoelectrochemical Water Splitting. *ChemSusChem* **2019**, *12*, 958. [CrossRef]
10. Feng, X.; Chen, Y.; Qin, Z.; Wang, M.; Guo, L. Facile Fabrication of Sandwich Structured WO_3 Nanoplate Arrays for Efficient Photoelectrochemical Water Splitting. *ACS Appl. Mater. Inter.* **2016**, *8*, 18089–18096. [CrossRef]
11. Li, S.; Zhao, Q.; Meng, D.; Wang, D.; Xie, T. Fabrication of metallic charge transfer channel between photoanode Ti/Fe_2O_3 and cocatalyst CoOx: An effective strategy for promoting photoelectrochemical water oxidation. *J. Mater. Chem. A* **2016**, *4*, 16661–16669. [CrossRef]

12. Zheng, B.-F.; Ouyang, T.; Wang, Z.; Long, J.; Chen, Y.; Liu, Z.-Q. Enhanced plasmon-driven photoelectrocatalytic methanol oxidation on Au decorated α-Fe_2O_3 nanotube arrays. *Chem. Commun.* **2018**, *54*, 9583–9586. [CrossRef] [PubMed]
13. Ma, H.; Ma, W.; Chen, J.-F.; Liu, X.-Y.; Peng, Y.-Y.; Yang, Z.-Y.; Tian, H.; Long, Y.-T. Quantifying visible-light-induced electron transfer properties of single dye-Sensitized ZnO entity for water splitting. *J. Am. Chem. Soc.* **2018**, *140*, 5272–5279. [CrossRef] [PubMed]
14. Lv, H.; Zhu, Q.; Zhang, M.; Yan, Y.; Liu, Y.; Li, M.; Yang, Z.; Geng, P. Synthesis of hexagonal ultrathin tungsten oxide nanowires with diameters below 5 nm for enhanced photocatalytic performance. *Superlattice. Microst* **2018**, *116*, 17–26.
15. Hu, J.; Duan, W.; He, H.; Lv, H.; Huang, C.; Ma, X. A promising strategy to tune the Schottky barrier of a $MoS_{2(1-x)}Se_{2x}$/graphene heterostructure by asymmetric Se doping. *J. Mater. Chem. C* **2019**, *7*, 7798–7805. [CrossRef]
16. Wu, P.; Liu, Z.; Chen, D.; Zhou, M.; Wei, J. Flake-like NiO/WO_3 p-n heterojunction photocathode for photoelectrochemical water splitting. *Appl. Surf. Sci.* **2018**, *440*, 1101–1106. [CrossRef]
17. Hua, X.; Ma, X.; Hu, J.; He, H.; Xu, G.; Huang, C.; Chen, X. Controlling electronic properties of MoS_2/graphene oxide heterojunctions for enhancing photocatalytic performance: The role of oxygen. *Phys. Chem. Chem. Phys.* **2018**, *20*, 1974–1983. [CrossRef]
18. Low, J.; Yu, J.; Jaroniec, M.; Wageh, S.; Al-Ghamdi, A.A. Heterojunction Photocatalysts. *Adv. Mater.* **2017**, *29*, 1601694. [CrossRef]
19. Luo, Z.; Li, C.; Zhang, D.; Wang, T.; Gong, J. Highly-oriented Fe_2O_3/$ZnFe_2O_4$ nanocolumnar heterojunction with improved charge separation for photoelectrochemical water oxidation. *Chem. Commun.* **2016**, *52*, 9013–9015. [CrossRef]
20. Peng, Y.; Lu, B.; Wu, F.; Zhang, F.; Lu, J.E.; Kang, X.; Ping, Y.; Chen, S. Point of Anchor: Impacts on Interfacial Charge Transfer of Metal Oxide Nanoparticles. *J. Am. Chem. Soc.* **2018**, *140*, 15290–15299. [CrossRef]
21. Bellani, S.; Ghadirzadeh, A.; Meda, L.; Savoini, A.; Tacca, A.; Marra, G.; Meira, R.; Morgado, J.; Di Fonzo, F.; Antognazza, M.R. Hybrid Organic/Inorganic Nanostructures for Highly Sensitive Photoelectrochemical Detection of Dissolved Oxygen in Aqueous Media. *Adv. Funct. Mater.* **2015**, *25*, 4531–4538. [CrossRef]
22. Wu, Q.; Li, L.; Hai, J.; Zhang, X.; Lu, Z.; Yang, J.; Liu, Y.; Zhang, L.; Zhan, C. Edge-to-face stacking non-fullerene small molecule acceptor for bulk heterojunction solar cells. *Dyes Pigment.* **2016**, *132*, 41–47. [CrossRef]
23. Lu, Z.; Jiang, B.; Zhang, X.; Tang, A.; Chen, L.; Zhan, C.; Yao, J. Perylene–Diimide Based Non-Fullerene Solar Cells with 4.34% Efficiency through Engineering Surface Donor/Acceptor Compositions. *Chem. Mater.* **2014**, *26*, 2907–2914. [CrossRef]
24. Sun, T.; Song, J.; Jia, J.; Li, X.; Sun, X. Real roles of perylenetetracarboxylic diimide for enhancing photocatalytic H_2-production. *Nano Energy* **2016**, *26*, 83–89. [CrossRef]
25. Zhang, K.; Wang, J.; Jiang, W.; Yao, W.; Yang, H.; Zhu, Y. Self-assembled perylene diimide based supramolecular heterojunction with Bi_2WO_6 for efficient visible-light-driven photocatalysis. *Appl. Catal. B Environ.* **2018**, *232*, 175–181. [CrossRef]
26. Nanda, K.K.; Swain, S.; Satpati, B.; Besra, L.; Mishra, B.; Chaudhary, Y.S. Enhanced Photocatalytic Activity and Charge Carrier Dynamics of Hetero-Structured Organic–Inorganic Nano-Photocatalysts. *ACS Appl. Mater. Interfaces* **2015**, *7*, 7970–7978. [CrossRef]
27. He, J.; Hagfeldt, A.; Lindquist, S.-E.; Grennberg, H.; Korodi, F.; Sun, L.; Akermark, B. Phthalocyanine-Sensitized Nanostructured TiO_2 Electrodes Prepared by a Novel Anchoring Method. *Langmuir* **2001**, *17*, 2743–2747. [CrossRef]
28. Lu, Z.; Zhan, C.; Yu, X.; He, W.; Jia, H.; Chen, L.; Tang, A.; Huang, J.; Yao, J. Large-scale, ultra-dense and vertically standing zinc phthalocyanine π–π stacks as a hole-transporting layer on an ITO electrode. *J. Mater. Chem.* **2012**, *22*, 23492–23496. [CrossRef]
29. Sapkota, K.P.; Lee, I.; Hanif, M.A.; Islam, M.A.; Hahn, J.R. Solar-Light-Driven Efficient ZnO–Single-Walled Carbon Nanotube Photocatalyst for the Degradation of a Persistent Water Pollutant Organic Dye. *Catalysts* **2019**, *9*, 498. [CrossRef]
30. Darensbourg, D.J.; Atnip, E.V.; Klausmeyer, K.K.; Reibenspies, J.H. Amino Acid Derivatives of Tungsten Carbonyl. Structure and Reactivity Investigations of Zerovalent Tungsten Glycine Derivatives. *Inorg. Chem.* **1994**, *33*, 5230–5237. [CrossRef]

31. Yao, H.; Domoto, K.; Isohashi, T.; Kimura, K. In Situ Detection of Birefringent Mesoscopic H and J Aggregates of Thiacarbocyanine Dye in Solution. *Langmuir* **2005**, *21*, 1067–1073. [CrossRef] [PubMed]
32. Zhang, X.; Lu, Z.; Ye, L.; Zhan, C.; Hou, J.; Zhang, S.; Jiang, B.; Zhao, Y.; Huang, J.; Zhang, S.; et al. A Potential Perylene Diimide Dimer-Based Acceptor Material for Highly Efficient Solution-Processed Non-Fullerene Organic Solar Cells with 4.03% Efficiency. *Adv. Mater.* **2013**, *25*, 5791–5797. [CrossRef] [PubMed]
33. Lv, H.; Yan, Y.; Zhang, M.; Tan, H.; Geng, P.; Le, S.; Yang, Z.; Liu, Y. The effects of adjusting pulse anodization parameters on the surface morphology and properties of a WO_3 photoanode for photoelectrochemical water splitting. *J. Solid State Electrochem.* **2018**, *22*, 2169–2181.